International Journal of Gravitation and Theoretical Physics
https://www.sciltp.com/journals/ijgtp

Article

Massive Scalar Clouds in the Dadhich-Maartens-Papadopoulos-Rezani Braneworld Spacetime

Ali Akyüz [1,2]

[1] Biomedical Device Technology Program, Bucak Emin Gülmez Vocational School of Technical Sciences, Burdur Mehmet Akif Ersoy University, 15300 Burdur, Türkiye; aakyuz@mehmetakif.edu.tr

[2] Bucak Faculty of Computer and Informatics, Burdur Mehmet Akif Ersoy University, 15300 Burdur, Türkiye

How To Cite: Akyüz, A. Massive Scalar Clouds in the Dadhich-Maartens-Papadopoulos-Rezani Braneworld Spacetime. *International Journal of Gravitation and Theoretical Physics* **2026**, *2*(3), 4. https://doi.org/10.53941/ijgtp.2026.100018

Received: 24 August 2026
Revised: 18 September 2026
Accepted: 21 September 2026
Published: 24 September 2026

Abstract: Massive-scalar quasi-bound states are studied around the static braneworld black hole whose exterior has the Reissner–Nordström form but contains a gravitational tidal charge rather than an electromagnetic charge. The tidal parameter is allowed to be negative, as favored by the original braneworld construction, as well as positive for comparison. The spectrum is obtained with a Frobenius–Leaver continued fraction and verified by independent integration from the horizon and infinity. Negative tidal charge enlarges the event horizon, reduces the field-mass range supporting an exterior potential well, and accelerates absorption. Positive tidal charge has the opposite effect and produces increasingly long-lived clouds. The real energies remain close to their hydrogen-like values, whereas the decay widths respond by factors that grow strongly with angular momentum. The same ordering persists along the first radial excitations, although the fractional response weakens slightly as the clouds extend farther from the horizon. The Schwarzschild spectrum, the hydrogenic limit, and the leading weak-binding tidal shift are all recovered. These results isolate the effect of a bulk-induced tidal field on gravitational atoms without rotation, electric coupling, or superradiant amplification.

Keywords: braneworld black holes; continued fractions; gravitational atoms; massive scalar fields; quasi-bound states; tidal charge

PACS: 04.50.-h; 04.70.Bw; 04.70.-s

1. Introduction

Extra-dimensional gravity can reproduce four-dimensional general relativity at long distances while modifying the strong-field region around compact objects. In the Randall–Sundrum construction, ordinary matter is confined to a three-brane embedded in a higher-dimensional bulk, whereas gravity can probe the additional dimension [1–3]. Projection of the bulk equations onto the brane introduces the electric part of the higher-dimensional Weyl tensor into the effective four-dimensional field equations [4]. The resulting nonlocal tidal field need not mimic any conventional four-dimensional matter source.

Dadhich, Maartens, Papadopoulos, and Rezania found a particularly transparent static solution of these effective equations [5]. Its line element has the algebraic form of the Reissner–Nordström geometry, but the coefficient of the inverse-square term is a tidal charge generated by the bulk. It is not the square of an electric charge and can therefore be negative. In the negative sector the bulk gravity strengthens the four-dimensional attraction, the event horizon lies outside the Schwarzschild radius, and no positive inner horizon is present. Positive values instead provide a useful Reissner–Nordström-like comparison.

Wave propagation has supplied several tests of braneworld black holes. Massless quasinormal modes, greybody factors, absorption, and the sensitivity of ringdown signals to tidal charge have been investigated in static and rotating settings [6–9]. Horizon-scale observations and other strong-field measurements have also been used to constrain tidal-charge parameters [10]. These scattering and ringing problems probe the response to radiation, but they do not determine the discrete levels of a massive field localized outside the horizon.

Although quasinormal modes of massive fields have been studied extensively across classical and modified black-hole backgrounds [11–21], their quasi-bound counterparts remain comparatively rare in the literature. This imbalance is particularly pronounced for non-Einstein and extra-dimensional geometries, for which an outgoing-wave spectrum may be known while the localized level structure has not yet been determined.

More precisely, Ref. [22] concentrated its quasi-bound-state analysis on the fundamental $\ell = m = 1$ mode of rotating, two-horizon braneworld black holes and on the resulting superradiant instability; the exactly spherical sector was explicitly left outside its parameter survey. The present work is therefore not the first braneworld quasi-bound-state calculation, but it supplies a distinct nonrotating baseline. In particular, it includes the physically preferred negative-b sector, which corresponds to positive tidal charge in the opposite sign convention of Ref. [22] and has only one positive horizon when the spin vanishes. It also resolves the fundamental monopole, dipole, and quadrupole levels and the first radial overtones, maps the multipole-dependent boundary for an exterior trapping well, derives the leading weak-binding tidal shift, and verifies selected continued-fraction roots by independent two-sided integration. These ingredients isolate ordinary horizon absorption and the radial level structure without contamination by rotational splitting or superradiant amplification.

Massive fields can form gravitational atoms: spatially extended clouds with complex frequencies whose real parts determine their energies and whose imaginary parts determine their absorption times [23–28]. Their outer boundary condition is exponential decay rather than outgoing radiation. Rotating braneworld gravitational atoms and their superradiant instability have recently been analyzed with continued fractions [22]. The static problem serves a different purpose: it removes rotational amplification and isolates how the tidal geometry changes binding, tunneling through the angular barrier, and horizon absorption.

Here we calculate the scalar quasi-bound spectrum of the static tidal-charge black hole over the negative, Schwarzschild, and positive sectors. We first identify the multipole-dependent parameter region in which the effective potential possesses an exterior well. A generalized Frobenius expansion then produces a five-term recurrence for nonzero tidal charge. Gaussian elimination reduces it to a three-term recurrence and a Leaver continued fraction. Selected frequencies are checked by an independent two-sided integration of the logarithmic derivative. We compute monopole, dipole, and quadrupole levels; their dependence on field mass and tidal charge; and the first two radial excitations. The Schwarzschild and weak-binding limits provide analytic and numerical accuracy tests.

Section 2 introduces the effective brane equations and the tidal-charge exterior. Section 3 formulates the scalar eigenvalue problem and its trapping condition. Section 4 develops the continued fraction and the independent validation. Section 5 presents the spectra, followed by the discussion and conclusions in Sections 6 and 7.

2. Tidal-Charge Black-Hole Geometry

We use geometrized natural units $G = c = \hbar = 1$ and the metric signature $(-,+,+,+)$. Length, time, inverse mass, and inverse frequency therefore carry the same unit, while the dimensionless products $M\mu_{\mathrm{s}}$ and $M\omega$ measure the gravitational coupling and mode frequency.

For a vacuum brane with vanishing four-dimensional cosmological constant, the projected field equations reduce to

$$G_{\mu\nu} = -\mathcal{E}_{\mu\nu}, \qquad \mathcal{E}^{\mu}{}_{\mu} = 0, \tag{1}$$

where $\mathcal{E}_{\mu\nu}$ is the electric projection of the bulk Weyl tensor. Equation (1) implies $R = 0$ but does not require $R_{\mu\nu} = 0$: the nonlocal bulk field can support an exterior geometry that is not a vacuum solution of the four-dimensional Einstein equations [4,5].

Here $G_{\mu\nu}$ is the four-dimensional Einstein tensor, $R_{\mu\nu}$ is the Ricci tensor, and R is its trace. Thus $\mathcal{E}_{\mu\nu}$ acts as a traceless effective stress tensor encoding nonlocal gravitational influence from the bulk rather than matter confined to the brane.

The static spherical solution is

$$ds^2 = -f(r)dt^2 + \frac{dr^2}{f(r)} + r^2 d\Omega^2, \tag{2}$$

$$f(r) = 1 - \frac{2M}{r} + \frac{q}{r^2}. \tag{3}$$

The angular element $d\Omega^2 = d\theta^2 + \sin^2\theta\, d\varphi^2$ is the metric of the unit two-sphere. The parameter M is both the ADM mass, which measures the total energy at spatial infinity, and the Komar mass associated with the timelike Killing symmetry. The coefficient q has dimensions of length squared and describes the tidal influence of the bulk;

it is unrelated to a Maxwell field. We introduce

$$b = \frac{q}{M^2}, \qquad x = \frac{r}{M}, \tag{4}$$

and restrict $b < 1$ so that the outer horizon is nondegenerate. The roots of f are

$$x_\pm = 1 \pm \sqrt{1-b}. \tag{5}$$

The corresponding areal radii are $r_\pm = Mx_\pm$; r_+ is the event horizon, while r_- is an inner horizon only when it is positive. For $b < 0$, $x_- < 0$ and only x_+ is a positive horizon. At $b = 0$ one recovers Schwarzschild with $x_+ = 2$. For $0 < b < 1$, both roots are positive and the geometry is algebraically identical to a subextremal Reissner–Nordström exterior. The surface gravity and temperature are

$$M\kappa_H = 2\pi M T_H = \frac{x_+ - x_-}{2x_+^2} = \frac{\sqrt{1-b}}{(1+\sqrt{1-b})^2}. \tag{6}$$

Both signs of b lower the temperature away from its Schwarzschild value when the mass is fixed, although they move the horizon in opposite directions.

The surface gravity κ_H measures the near-horizon redshift gradient, and $T_H = \kappa_H/(2\pi)$ is the associated Hawking temperature. The limit $b \to 1^-$ makes x_+ and x_- coincide and sends κ_H to zero; this degenerate limit is the positive-charge extremal endpoint referred to below.

3. Massive-Scalar Eigenvalue Problem

The scalar field of mass μ_s satisfies

$$(\Box - \mu_\mathrm{s}^2)\Phi = 0. \tag{7}$$

Here Φ is the test scalar and $\Box = g^{\mu\nu}\nabla_\mu\nabla_\nu$ is the covariant wave operator. The test-field approximation means that the stress energy of Φ does not alter the background geometry. The mass μ_s is equivalently the inverse Compton wavelength of the field in the units used here. With scalar spherical harmonics $Y_{\ell m}$ and time dependence $e^{-i\omega t}$, write

$$\Phi = e^{-i\omega t} Y_{\ell m}(\theta,\varphi)\frac{u(r)}{r}. \tag{8}$$

The integer $\ell = 0, 1, 2, \ldots$ is the orbital multipole number, conventionally called monopole, dipole, and quadrupole for the first three values; m is the azimuthal number. Spherical symmetry makes the spectrum independent of m. The function $u(r)$ is the reduced radial amplitude, with the factor $1/r$ removed so that its equation takes one-dimensional wave form. Introducing $dr_*/dr = f^{-1}$ gives a Schrödinger-type radial equation,

$$\frac{d^2u}{dr_*^2} + [\omega^2 - V_\ell(r)]u = 0, \tag{9}$$

$$V_\ell(r) = f(r)\left[\mu_\mathrm{s}^2 + \frac{\ell(\ell+1)}{r^2} + \frac{f'(r)}{r}\right]. \tag{10}$$

The tortoise coordinate r_* stretches the exterior so that the event horizon is at $r_* \to -\infty$ and spatial infinity at $r_* \to +\infty$. A prime on f denotes differentiation with respect to the areal radius r. In V_ℓ, the three bracketed contributions represent the scalar rest mass, the centrifugal barrier, and the curvature-induced radial term, respectively.

3.1 Quasi-Bound Boundary and Trapping Conditions

Define the dimensionless frequency and field coupling by $\widehat{\omega} = M\omega$ and $\alpha = M\mu_\mathrm{s}$. A quasi-bound state is ingoing at the future horizon and decays at spatial infinity,

$$u \sim \begin{cases} e^{-i\omega r_*}, & r \to r_+^+, \\ e^{-kr} r^\nu, & r \to \infty, \end{cases} \tag{11}$$

where

$$k = \sqrt{\mu_s^2 - \omega^2} = M^{-1}\sqrt{\alpha^2 - \widehat{\omega}^2}, \qquad \nu = \frac{2\widehat{\omega}^2 - \alpha^2}{\sqrt{\alpha^2 - \widehat{\omega}^2}}. \tag{12}$$

We write $\omega = \omega_R + i\omega_I$. The real part ω_R is the oscillation frequency and therefore the level energy per quantum, whereas $\omega_I < 0$ describes temporal damping. We use $\Gamma = -\omega_I > 0$ for the decay width and $\tau = 1/\Gamma$ for the e-folding lifetime. The coupling $\alpha = M\mu_\mathrm{s}$ compares the black-hole length scale with the scalar Compton wavelength, while $\widehat{\omega} = M\omega$ is the frequency in inverse-black-hole-mass units. The quantity k is the inverse radial localization length of the outer tail, and ν is the power-law correction produced by the long-range gravitational field. The square-root branch is selected with positive real part. Exponential decay requires $\omega_R < \mu_\mathrm{s}$. In contrast, a quasinormal mode is outgoing at infinity and describes radiative ringing rather than a localized cloud.

The distinction is entirely in the spectral boundary conditions, not in the radial differential equation. With the same time dependence $e^{-i\omega t}$, both problems select the ingoing solution at the future horizon. At infinity, however, a quasinormal mode selects the outgoing branch

$$u_\mathrm{QNM} \sim \begin{cases} e^{-i\omega r_*}, & r_* \to -\infty, \\ e^{+ipr_*}, & r_* \to +\infty, \end{cases} \qquad p = \sqrt{\omega^2 - \mu_\mathrm{s}^2}, \tag{13}$$

up to the long-range power-law factor. The branch of p is fixed by outgoing propagation and then analytically continued to complex frequency. A quasi-bound state instead takes $p = ik$ with $\mathrm{Re}\, k > 0$ and retains the exponentially decreasing solution in Equation (11). It therefore carries no outward wave flux at spatial infinity; in the present static geometry its negative imaginary part is generated by leakage through the inner barrier and absorption at the horizon. A quasinormal mode loses energy both into the horizon and through outgoing radiation at infinity. Consequently, quasinormal modes do not require a potential well or $\omega_R < \mu_\mathrm{s}$, whereas a localized quasi-bound state requires both the decaying branch and the trapping conditions stated below. Figure 1 summarizes this difference.

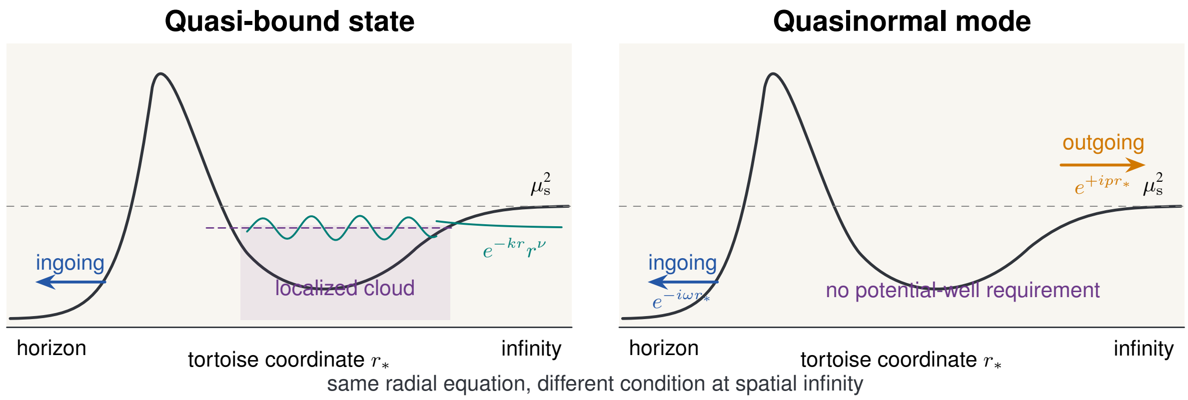

Figure 1. Schematic comparison of the two spectral problems for the same radial operator. Both solutions are ingoing at the future horizon. A quasi-bound state occupies an exterior well and decays exponentially at infinity, while a quasinormal mode is defined by an outgoing wave there and does not require a trapping well. The curves and arrows illustrate the boundary conditions rather than a particular numerical mode.

Spatial decay is necessary but not sufficient for a gravitational atom. The potential must have an exterior maximum followed by a minimum, and the real mode energy must lie between them (see Figure 2),

$$V_\mathrm{min} < \omega_R^2 < V_\mathrm{max}. \tag{14}$$

The inner maximum supplies the barrier separating the cloud from the absorbing horizon, while the minimum identifies the storage region.

In dimensionless form, with $L = \ell(\ell+1)$,

$$M^2 V_\ell = f(x)\left[\alpha^2 + \frac{L}{x^2} + \frac{2}{x^3} - \frac{2b}{x^4}\right]. \tag{15}$$

The abbreviation L is the eigenvalue of the angular Laplacian on the unit two-sphere. The quantities V_max and V_min denote, respectively, the inner barrier height and the bottom of the exterior storage well. At a stationary point, $dV_\ell/dx = 0$ can be solved for the coupling,

$$\begin{aligned} \alpha^2 = \mathcal{G}_\ell(x,b) = \big[&Lx^4 + 3(1-L)x^3 + 2(bL - 4 - 2b)x^2 \\ &+ 15bx - 6b^2\big]\big/\big[x^4(x-b)\big]. \end{aligned} \tag{16}$$

The function $\mathcal{G}_\ell(x, b)$ is an auxiliary geometrical relation: at each stationary radius it gives the squared coupling α^2 for which that stationary point occurs. The maximum of $\mathcal{G}_\ell$ for $x > x_+$ determines the critical coupling at which the exterior maximum and minimum merge. We apply both this geometrical condition and Equation (14) to every frequency retained below.

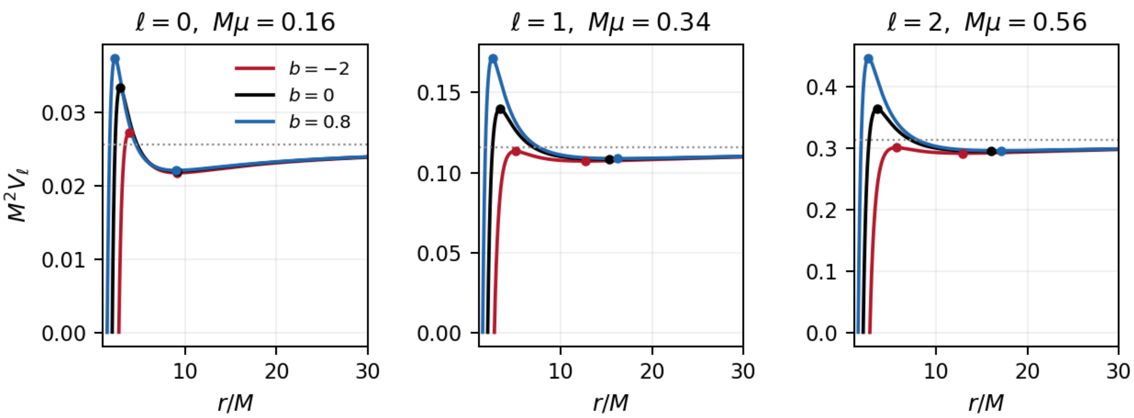

Figure 2. Dimensionless effective potential for monopole, dipole, and quadrupole fields. Negative tidal charge moves the horizon outward and lowers the inner barrier; positive charge moves it inward and raises the barrier. The dotted line is the asymptotic value $M^2\mu_s^2$, and the points mark the exterior maximum and minimum. Different couplings are used so that each multipole is displayed close to the upper common range analyzed for all three geometries.

In Table 1, the three columns headed by ℓ give the critical value $(M\mu_s)_{\rm well}$ at which the barrier and well merge; trapping is possible below this geometrical threshold.

Table 1. Outer horizon and critical potential-well couplings.

b	r_+/M	$\ell = 0$	$\ell = 1$	$\ell = 2$
-2	2.7321	0.2145	0.3817	0.6072
-1	2.4142	0.2298	0.4152	0.6600
0	2.0000	0.2500	0.4656	0.7401
0.5	1.7071	0.2625	0.5045	0.8025
0.8	1.4472	0.2704	0.5374	0.8562
0.9	1.3162	0.2728	0.5513	0.8791

The links between various parameters of the configuration are shown in Figure 3.

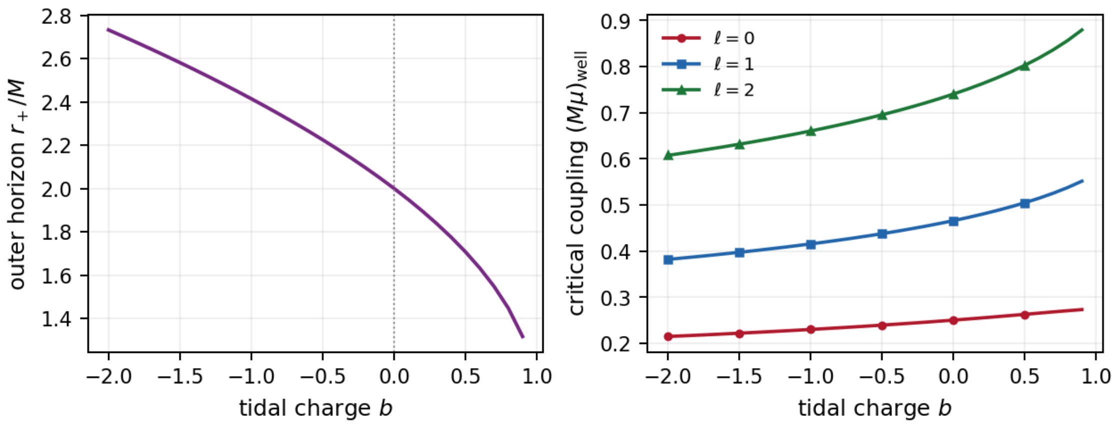

Figure 3. Left: outer-horizon radius as a function of tidal charge. **Right:** critical field coupling below which the effective potential possesses a distinct exterior maximum and minimum. Negative tidal charge enlarges the horizon and narrows the trapping range, while the positive sector does the reverse.

3.2 Weak-Binding Spectrum

The inverse-radius part of g_{tt} is independent of b, so the leading hydrogenic energy is unchanged. With principal quantum number $N = n_r + \ell + 1$,

$$\frac{\omega_R}{\mu_{\rm s}} = 1 - \frac{\alpha^2}{2N^2} + O(\alpha^4). \tag{17}$$

The nonnegative integer $n_r = 0, 1, 2, \ldots$ is the radial overtone number and counts radial nodes of the cloud outside the horizon; $n_r = 0$ is the fundamental radial level. Thus N is the usual hydrogenic principal quantum number. The tidal charge first contributes through the weak-field Newtonian potential correction $\delta\Phi_{\rm N} = bM^2/(2r^2)$, obtained from $g_{tt} \simeq -(1 + 2\Phi_{\rm N})$. First-order perturbation theory with hydrogenic wave functions gives

$$\frac{\omega_R(b) - \omega_R(0)}{\mu_{\rm s}} = \frac{b\alpha^4}{2N^3(\ell + 1/2)} + O(\alpha^6). \tag{18}$$

Thus the leading tidal energy shift is negative for the physical negative charge and positive for the Reissner–Nordström-like sector. Its fourth-order scaling makes the energy shift much smaller than the corresponding change in decay width.

4. Frobenius–Leaver Calculation

The two regular singular points associated with the roots of f motivate the compact coordinate

$$z = \frac{x - x_+}{x - x_-}, \qquad x = \frac{x_+ - x_- z}{1 - z}. \tag{19}$$

It maps the event horizon to $z = 0$ and infinity to $z = 1$, including when $x_- < 0$. Define

$$\delta = x_+ - x_-, \quad K = \sqrt{\alpha^2 - \widehat{\omega}^2}, \quad \rho = -\frac{i\widehat{\omega} x_+^2}{\delta}. \tag{20}$$

Here δ is the dimensionless separation of the two roots, $K = Mk$ is the dimensionless inverse decay length, and ρ is the ingoing Frobenius exponent determined by the near-horizon phase. After removing the required behavior at both boundaries, the radial amplitude is written as

$$u = e^{-Kx} z^{\rho} (1 - z)^{-\nu} \sum_{n=0}^{\infty} a_n z^n, \qquad \nu = \frac{2\widehat{\omega}^2 - \alpha^2}{K}. \tag{21}$$

The numbers a_n are the coefficients of the remaining regular Frobenius series, with $n = 0, 1, 2, \ldots$ the series index. Because the radial equation is linear, their overall normalization is arbitrary; the numerical calculation fixes $a_0 = 1$.

For clarity, let $q_z = 1 - z$ and $\mathcal{R}_z = x_+ - x_- z$. Before inserting the prefactor in Equation (21), the transformed radial equation can be written as

$$A_0 u'' + B_0 u' + C_0 u = 0, \tag{22}$$

where primes now denote z derivatives and

$$\begin{aligned} A_0 &= \delta^2 z^2 q_z^4 \mathcal{R}_z^2, \\ B_0 &= \delta^2 z q_z^4 \mathcal{R}_z^2 - 2\delta^3 z^2 q_z^3 \mathcal{R}_z, \\ C_0 &= \widehat{\omega}^2 \mathcal{R}_z^6 - \delta^2 \alpha^2 z \mathcal{R}_z^4 - \delta^2 L z q_z^2 \mathcal{R}_z^2 \\ &\quad - \delta^3 z q_z^2 \mathcal{R}_z (1 + z) + 2\delta^4 z^2 q_z^2. \end{aligned} \tag{23}$$

The abbreviations q_z and $\mathcal{R}_z$ are auxiliary polynomials that keep the compactified equation finite. The functions A_0, B_0, and C_0 are respectively the coefficients of the second derivative, first derivative, and undifferentiated radial amplitude before its known boundary factors are removed. If $g = \rho/z + \nu/q_z - K\delta/q_z^2$ is the logarithmic derivative of the prefactor, the regular series $S = \sum a_n z^n$ obeys

$$AS'' + BS' + CS = 0, \tag{24}$$

$$\begin{aligned} A &= A_0, \qquad B = 2A_0 g + B_0, \\ C &= A_0(g' + g^2) + B_0 g + C_0. \end{aligned} \tag{25}$$

Thus g encodes only the analytically extracted horizon and infinity behavior, while S is regular on the compact interval $0 \le z \le 1$. The new coefficient polynomials A, B, and C act on S'', S', and S, respectively. The indicial and asymptotic choices leave a common factor $z(1-z)^2$. After dividing it out, A, B, and C have degrees five, four, and three for $b \neq 0$. Matching powers of z therefore gives a five-term recurrence. Writing the coefficient of z^j in each polynomial as A_j, B_j, and C_j, its compact exact form is

$$\begin{aligned} \sum_j \big[& A_j(n-j+2)(n-j+1)a_{n-j+2} \\ & + B_j(n-j+1)a_{n-j+1} + C_j a_{n-j}\big] = 0. \end{aligned} \tag{26}$$

Terms with negative indices are omitted. At $b = 0$, the degrees fall to three, two, and one and Equation (26) becomes the standard Schwarzschild three-term recurrence directly.

Successive Gaussian eliminations reduce the general relation to

$$\widetilde{A}_n a_{n+1} + \widetilde{B}_n a_n + \widetilde{C}_n a_{n-1} = 0. \tag{27}$$

The tilded quantities are the three Gaussian-eliminated recurrence coefficients; they should not be confused with the physical coupling $\alpha = M\mu_{\rm s}$. The minimal solution, which converges at $z = 1$ and hence satisfies the decaying outer condition, is selected by Leaver's continued fraction [29,30],

$$\widetilde{B}_0 - \cfrac{\widetilde{A}_0\widetilde{C}_1}{\widetilde{B}_1 - \cfrac{\widetilde{A}_1\widetilde{C}_2}{\widetilde{B}_2 - \cfrac{\widetilde{A}_2\widetilde{C}_3}{\widetilde{B}_3 - \cdots}}} = 0. \tag{28}$$

Complex roots are followed continuously in b, α, and n_r. The calculations use between 650 and 1400 recurrence coefficients, with larger orders near the positive extremal limit. This number is the continued-fraction truncation order: increasing it retains more Frobenius coefficients and tests convergence of the computed root.

4.1 Independent Two-Sided Integration

As a separate numerical check, define the Riccati variable $\mathcal{Y} = u'/u$, where the prime now again denotes an areal-radius derivative. From Equation (9),

$$\mathcal{Y}' + \mathcal{Y}^2 + \frac{f'}{f}\mathcal{Y} + \frac{\omega^2}{f^2} - \frac{\mu_{\rm s}^2}{f} - \frac{L}{r^2 f} - \frac{f'}{rf} = 0. \tag{29}$$

The logarithmic derivative $\mathcal{Y}$ removes the arbitrary normalization of u, so the eigenfrequency can be found by equating the outward and inward values of a single complex quantity. An outward integration initialized with the ingoing horizon series and an inward integration initialized with the decaying asymptotic series are matched at an intermediate radius. The explicit boundary coefficients are listed in Appendix A. This procedure does not use the Frobenius recurrence and is therefore sensitive to different numerical errors.

5. Numerical Spectra

5.1 Validation and Analytic Limits

Throughout the numerical discussion, the superscript "Schw" denotes the $b = 0$ Schwarzschild value. The dimensionless frequency difference $\Delta\widehat{\omega} = M(\omega_{\rm CF} - \omega_{\rm match})$ compares the continued-fraction and independent matching calculations.

The Schwarzschild limit is recovered both algebraically, through the collapse of the five-term recurrence, and numerically. For example, at $M\mu_{\rm s} = 0.14$ the fundamental Schwarzschild frequencies are $M\omega = 0.1383750588 - 1.587733 \times 10^{-4} i$ for $\ell = 0$ and $M\omega = 0.1396494941 - 5.655878 \times 10^{-10} i$ for $\ell = 1$. These values also agree with the independent integration, as demonstrated by the comparison in Table 2.

Table 2. Comparison of the continued-fraction and two-sided integration methods. The table lists the continued-fraction frequency and the absolute differences between the methods.

b	ℓ	$M\mu_s$	$M\omega_R$	$-M\omega_I$	$\lvert\Delta\widehat{\omega}_R\rvert$	$\lvert\Delta\widehat{\omega}_I\rvert$
-2	0	0.14	0.1383040436	3.006655×10^{-4}	0	0
-2	1	0.14	0.1396444872	3.800428×10^{-9}	2.8×10^{-17}	2.1×10^{-17}
-2	2	0.30	0.2984012502	1.334119×10^{-9}	1.7×10^{-16}	1.1×10^{-17}
0	0	0.14	0.1383750588	1.587733×10^{-4}	3.6×10^{-14}	4.8×10^{-14}
0	1	0.14	0.1396494941	5.655878×10^{-10}	1.1×10^{-16}	3.0×10^{-18}
0	2	0.30	0.2984440721	4.901853×10^{-11}	2.2×10^{-16}	9.5×10^{-19}
0.8	0	0.14	0.1384026300	9.820561×10^{-5}	2.8×10^{-17}	2.2×10^{-19}
0.8	1	0.14	0.1396514495	6.513217×10^{-11}	1.7×10^{-16}	8.9×10^{-18}
0.8	2	0.30	0.2984604567	1.431309×10^{-12}	2.2×10^{-16}	5.7×10^{-20}

Figure 4 tests the weak-binding expansion. The ordinary hydrogenic term is approached for every tidal charge. More stringently, the difference between a charged geometry and Schwarzschild follows the sign, angular dependence, and fourth-power scaling predicted by Equation (18). This comparison resolves a correction that is far smaller than the total relativistic binding energy.

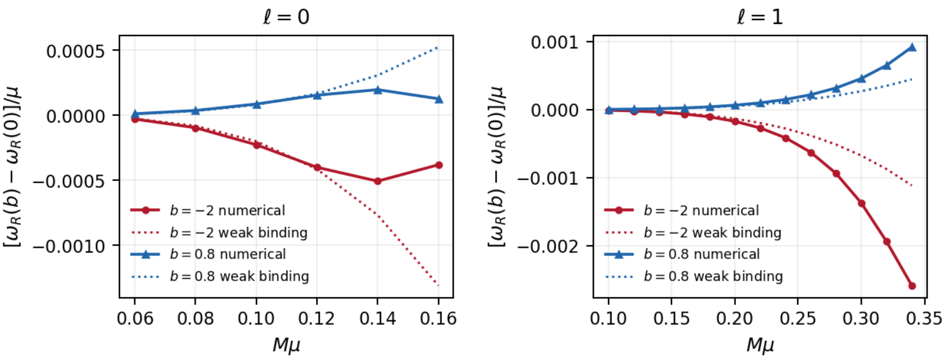

Figure 4. Tidal contribution to the real frequency for the fundamental monopole and dipole. Solid curves are continued-fraction data and dotted curves are the weak-binding result in Equation (18). Agreement improves toward small field coupling.

5.2 Fundamental Levels and Tidal-Charge Response

Figure 5 and Table 3 show the lowest radial state. Negative tidal charge lowers the real frequencies and increases every width considered. At $b = -2$, relative to Schwarzschild, the monopole energy changes by only -0.0513% while its width grows by a factor 1.89. The dipole energy changes by -0.00359% and its width by a factor 6.72. For the quadrupole at $M\mu_s = 0.30$, the energy shift is -0.0143% but the width grows by a factor 27.2.

Positive tidal charge reverses the trend. At $b = 0.8$, the corresponding width ratios are 0.619, 0.115, and 0.0292 for $\ell = 0$, 1, and 2. Nearer the extremal endpoint, at $b = 0.9$, the dipole and quadrupole widths fall to 5.54% and 0.952% of their Schwarzschild values. The real shifts remain below 0.021% throughout the displayed fundamental sequences.

Table 3. Fundamental quasi-bound frequencies. The monopole and dipole use $M\mu_s = 0.14$; the quadrupole uses $M\mu_s = 0.30$.

	$\ell = 0$		$\ell = 1$		$\ell = 2$	
b	$M\omega_R$	$-M\omega_I$	$M\omega_R$	$-M\omega_I$	$M\omega_R$	$-M\omega_I$
-2	0.138304044	3.007×10^{-4}	0.139644487	3.800×10^{-9}	0.298401250	1.334×10^{-9}
-1	0.138337336	2.302×10^{-4}	0.139647012	1.790×10^{-9}	0.298423005	3.542×10^{-10}
0	0.138375059	1.588×10^{-4}	0.139649494	5.656×10^{-10}	0.298444072	4.902×10^{-11}
0.5	0.138393961	1.216×10^{-4}	0.139650719	2.056×10^{-10}	0.298454360	9.080×10^{-12}
0.8	0.138402630	9.821×10^{-5}	0.139651449	6.513×10^{-11}	0.298460457	1.431×10^{-12}
0.9	0.138403602	9.067×10^{-5}	0.139651692	3.135×10^{-11}	0.298462476	4.669×10^{-13}

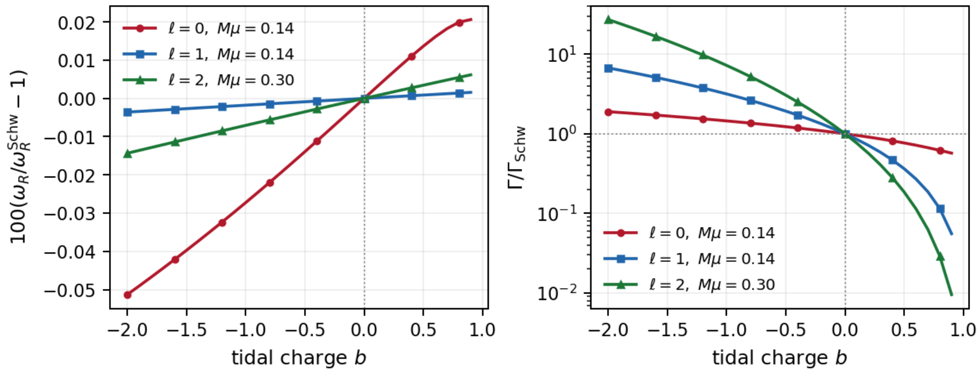

Figure 5. Fundamental scalar levels versus tidal charge. The **left panel** shows the percentage real-frequency shift from Schwarzschild, and the **right panel** shows the decay width normalized by its Schwarzschild value. Negative tidal charge enhances absorption, increasingly strongly with angular momentum; positive charge suppresses it.

5.3 Dependence on Field Mass

The mass scans in Figure 6 are restricted to modes that satisfy Equation (14) for all three displayed geometries. The common intervals are $0.06 \le M\mu_{\mathrm{s}} \le 0.16$ for monopoles, $0.10 \le M\mu_{\mathrm{s}} \le 0.34$ for dipoles, and $0.24 \le M\mu_{\mathrm{s}} \le 0.56$ for quadrupoles. Binding strengthens and decay accelerates as the scalar mass increases. The tidal splitting of the real energies remains difficult to see on the scale of the total binding, whereas the width curves remain widely separated.

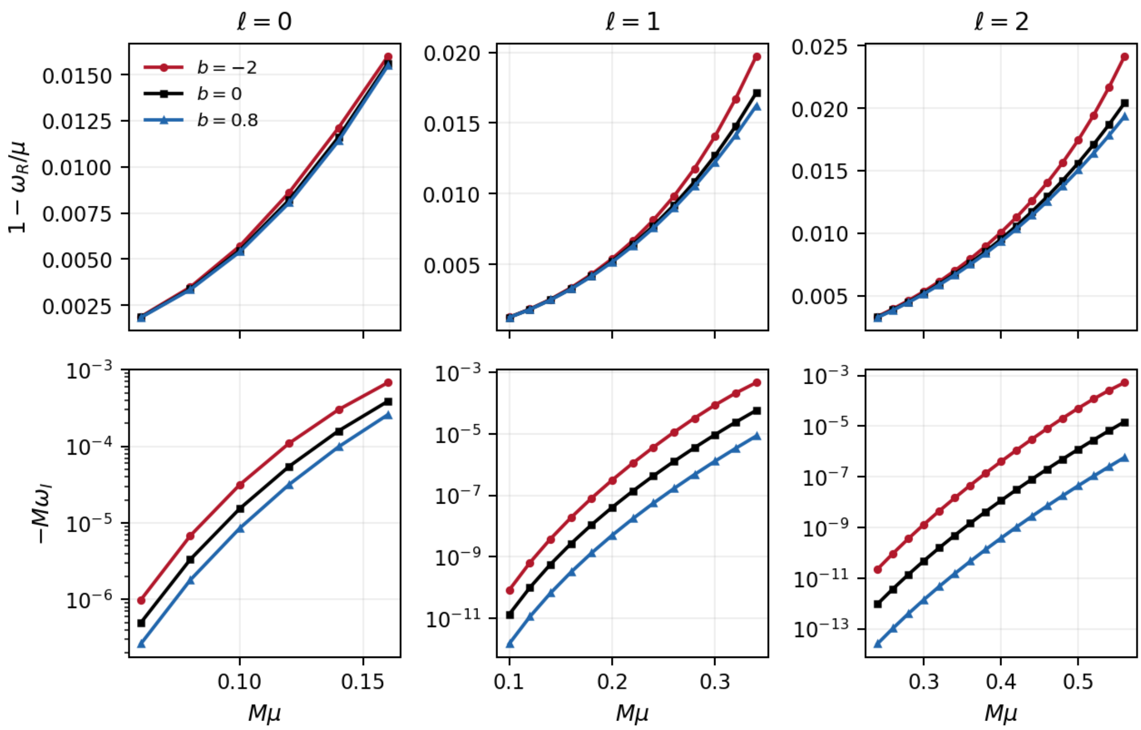

Figure 6. Fundamental binding energies (**top**) and decay widths (**bottom**) as functions of field mass. The horizontal ranges are chosen so that every plotted frequency lies inside an exterior potential well.

The plotted quantity $1-\omega_R/\mu_{\mathrm{s}}$ is the binding energy as a fraction of the scalar rest energy, while $-M\omega_I = M\Gamma$ is the dimensionless decay width.

The weak-coupling width follows the familiar centrifugal hierarchy. Fits over the lowest available masses approach the Schwarzschild powers $\Gamma \propto (M\mu_{\mathrm{s}})^{4\ell+6}$, while tidal charge changes primarily the coefficient. Departures of the fitted slopes from the asymptotic integers at the displayed masses reflect finite-coupling corrections rather than a new power law.

5.4 Radial Excitations

Figure 7 follows $n_r = 0, 1, 2$ at fixed angular momentum. Increasing n_r moves the real frequency toward the rest-mass threshold and reduces the absolute width. The tidal response does not grow with radial overtone number. For $\ell = 0$, the width enhancement at $b = -2$ decreases from 1.89 for the ground state to 1.79 for $n_r = 2$; the ratio at $b = 0.8$ changes from 0.619 to 0.635. For $\ell = 1$, the corresponding sequences are 6.72 to 6.63 and 0.1152 to 0.1158. Higher bound levels are more extended and consequently sample the short-range tidal deformation slightly less strongly.

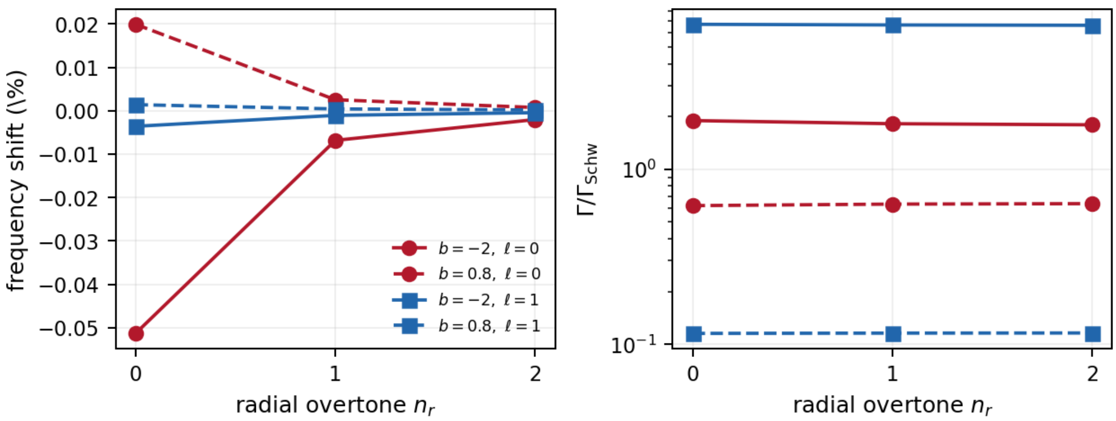

Figure 7. Tidal shifts along the first three radial levels at $M\mu_s = 0.14$. The solid curves show negative tidal charge and the dashed curves positive charge. The real-frequency response decreases with n_r, while the normalized width response is nearly constant and moves slightly toward unity.

6. Discussion

The contrast between energies and lifetimes follows from the radial location of the tidal correction. The coefficient of the asymptotic $1/r$ attraction is always M, so the leading hydrogenic spectrum is common to every value of b. Tidal charge enters at order $1/r^2$, producing the fourth-order weak-binding shift in Equation (18). The cloud energy is therefore anchored mainly by the universal far field.

Absorption probes a different part of the geometry. Negative tidal charge moves the horizon outward and lowers the potential barrier separating the cloud from it. The wave reaching the horizon is consequently larger, which explains the enhanced widths. This agrees qualitatively with the greater massless absorption found for braneworld black holes [6]. The enhancement grows with ℓ because a small change in the centrifugal tunneling exponent produces a large fractional change in an already narrow higher-multipole width. Positive b raises the barrier and shrinks the horizon, strongly suppressing absorption as the extremal limit is approached.

The surface gravity alone does not control these widths. At $b = -2$, for example, $M\kappa_H = 0.2321$ is below the Schwarzschild value 0.25, yet all three widths are larger. The relevant quantity is the full transmission from the well through the barrier to the ingoing horizon, not a local thermal scale. The potential-well boundary also carries independent information: negative tidal charge reduces the maximum scalar mass that can be trapped, even while it accelerates the decay of the states that remain.

Because the test scalar is uncharged, the positive-b sector is sensitive only to the Reissner–Nordström geometry; there is no electrostatic term in the wave equation. Charged scalar fields around electrically charged black holes have additional Coulomb and superradiant effects [31–33]. Those mechanisms are absent here. Likewise, the static tidal-charge spacetime has no ergoregion, so every computed mode decays. Rotation can reverse the horizon flux and generate superradiant braneworld clouds [22]; the present results supply the nonrotating absorption baseline against which that growth can be separated.

Unlike some quasinormal spectra, the radial quasi-bound overtones do not become increasingly sensitive to the short-range modification. Their larger spatial extent reduces the real-frequency shift and makes the width ratio drift mildly back toward its Schwarzschild value. Angular momentum, not radial overtone number, is the more efficient amplifier of tidal-charge effects in the present spectrum.

The analysis treats the scalar as a test field and the four-dimensional exterior as fixed. It does not determine the continuation into the bulk or the backreaction of a macroscopically occupied cloud. Observational bounds on tidal charge are also model dependent, so the interval displayed here is intended to resolve the spectral systematics rather than to impose a single astrophysical prior. Time-domain excitation amplitudes, rotating extensions, and self-consistent bulk perturbations remain natural next steps.

7. Conclusions

Quasinormal modes of higher-dimensional and braneworld black holes have been examined in many static and rotating models [6–9,34–36]. By comparison, quasi-bound-state spectra in these geometries remain much less developed, with rotating braneworld gravitational atoms providing one of the few detailed examples [22].

We have calculated massive-scalar quasi-bound states of the static tidal-charge black hole using a generalized Frobenius–Leaver method. A nonzero tidal charge produces a five-term recurrence, which is reduced to a three-term continued fraction. Independent logarithmic-derivative matching confirms the complex frequencies, and the Schwarzschild, hydrogenic, and leading weak-binding tidal limits are recovered.

Negative tidal charge strengthens horizon absorption while leaving the energies nearly hydrogenic. Across the fundamental states examined, the energy shifts remain below a few hundredths of a percent, but the widths can increase from a factor of order two for the monopole to more than an order of magnitude for the quadrupole. Positive tidal charge reverses the effect and can suppress higher-multipole widths by two orders of magnitude before the extremal endpoint. The response persists along the radial ladder but becomes slightly weaker for more extended overtones.

The potential-well analysis adds a complementary restriction: negative tidal charge lowers the largest field coupling for which trapping is possible, whereas positive charge enlarges that range. Tidal-charge gravitational atoms thus separate two aspects of the bulk-induced geometry. Their real energies measure the nearly universal long-range attraction, while their lifetimes resolve the horizon position and short-range tunneling barrier.

Funding

This research received no external funding.

Institutional Review Board Statement

Not applicable.

Informed Consent Statement

Not applicable.

Data Availability Statement

The numerical data and scripts used to generate the spectra, tables, and figures are included with the article source files.

Acknowledgments

The author is grateful to Bekir Can Lütfüoğlu for stimulating discussions during academic visits in 2025, from which the initial idea for this work emerged.

Conflicts of Interest

The authors declare no conflict of interest.

Use of AI and AI-Assisted Technologies

No AI tools were utilized for this paper.

Appendix A. Boundary Expansions for Matching

All quantities in this appendix use $M = 1$. Let $y = r - r_+$ near the event horizon and expand

$$f = f_1 y + f_2 y^2 + O(y^3), \quad f_1 = \frac{r_+ - r_-}{r_+^2}, \quad f_2 = -\frac{2}{r_+^3} + \frac{3b}{r_+^4}. \tag{A1}$$

Thus y is the areal-coordinate distance from the horizon, $f_1 = f'(r_+)$ is twice the surface gravity in these units, and $f_2 = f''(r_+)/2$ is the quadratic Taylor coefficient of the lapse. The ingoing solution is

$$u = y^\rho (1 + c_1 y + O(y^2)), \qquad \rho = -\frac{i\omega}{f_1}. \tag{A2}$$

The coefficient c_1 is the first regular correction to the leading ingoing power y^ρ. Writing the radial equation as $u'' + Pu' + Qu = 0$, define

$$\begin{aligned} p_0 &= \frac{f_2}{f_1}, \\ q_{-2} &= \frac{\omega^2}{f_1^2} = -\rho^2, \\ q_{-1} &= -2q_{-2}\frac{f_2}{f_1} - \frac{\mu_s^2 + \ell(\ell+1)/r_+^2}{f_1} - \frac{1}{r_+}. \end{aligned} \tag{A3}$$

Here $P(r)$ and $Q(r)$ multiply the first-derivative and undifferentiated terms in the areal-coordinate equation. The subscripts on p_0, q_{-2}, and q_{-1} identify the corresponding power of y in their near-horizon expansions. Then

$$c_1 = -\frac{p_0\rho + q_{-1}}{2\rho + 1}, \qquad \mathcal{Y}(r_+ + \epsilon) = \frac{\rho}{\epsilon} + c_1 + O(\epsilon). \tag{A4}$$

The positive regulator $\epsilon \ll r_+$ places the numerical starting point just outside the horizon, avoiding the coordinate singularity itself.

At large radius,

$$u = e^{-kr} r^\nu \left(1 + \frac{c_\infty}{r} + O(r^{-2})\right). \tag{A5}$$

The coefficient c_∞ is the first inverse-radius correction to the decaying outer tail. The required coefficient expansions are

$$\begin{aligned} P &= \frac{2}{r^2} + O(r^{-3}), \\ Q &= -k^2 + \frac{2k\nu}{r} + \frac{q_2}{r^2} + O(r^{-3}), \\ q_2 &= \omega^2(12 - 2b) - \mu_s^2(4 - b) - \ell(\ell+1). \end{aligned} \tag{A6}$$

The symbol q_2 denotes the coefficient of r^{-2} in the large-radius expansion of $Q(r)$; it is unrelated to the dimensional tidal charge q in Equation (3). Matching powers gives

$$\begin{aligned} c_\infty &= -\frac{\nu^2 - \nu - 2k + q_2}{2k}, \\ \mathcal{Y}(R_\infty) &= -k + \frac{\nu}{R_\infty} - \frac{c_\infty}{R_\infty^2} + O(R_\infty^{-3}). \end{aligned} \tag{A7}$$

The validation runs use $r_m = 9M$, $R_\infty = 1100M$, relative tolerance 6×10^{-12}, and absolute tolerance 6×10^{-14}. Here R_∞ is the finite radius at which the inward integration is initialized, and r_m is the intermediate radius where the two logarithmic derivatives are required to agree. The relative and absolute tolerances control the adaptive integration error.

References

1. Randall, L.; Sundrum, R. Large Mass Hierarchy from a Small Extra Dimension. *Phys. Rev. Lett.* **1999**, *83*, 3370–3373. https://doi.org/10.1103/physrevlett.83.3370.
2. Randall, L.; Sundrum, R. An alternative to compactification. *Phys. Rev. Lett.* **1999**, *83*, 4690–4693. https://doi.org/10.1103/physrevlett.83.4690.
3. Maartens, R.; Koyama, K. Brane-world gravity. *Living Rev. Relativ.* **2010**, *13*, 5. https://doi.org/10.12942/lrr-2010-5.
4. Shiromizu, T.; Maeda, K.I.; Sasaki, M. The Einstein equations on the 3-brane world. *Phys. Rev. D* **2000**, *62*, 024012. https://doi.org/10.1103/physrevd.62.024012.
5. Dadhich, N.; Maartens, R.; Papadopoulos, P.; et al. Black holes on the brane. *Phys. Lett. B* **2000**, *487*, 1–6. https://doi.org/10.1016/s0370-2693(00)00798-x.
6. Toshmatov, B.; Stuchlík, Z.; Schee, J.; et al. Quasinormal frequencies of black hole in the braneworld. *Phys. Rev. D* **2016**, *93*, 124017. https://doi.org/10.1103/physrevd.93.124017.
7. Abbasvandi, N.; Soleimani, M.J.; Abdullah, W.A.T.W.; et al. Quasinormal Modes of Charged Black Holes Localized in the Randall-Sundrum Brane World. *arXiv* **2016**, arXiv:1610.04526. http://arxiv.org/abs/1610.04526v3.
8. Dey, R.; Chakraborty, S.; Afshordi, N. Echoes from braneworld black holes. *Phys. Rev. D* **2020**, *101*, 104014. https://doi.org/10.1103/physrevd.101.104014.

9. Zinhailo, A.F. Exploring unique quasinormal modes of a massive scalar field in brane-world scenarios. *Phys. Lett. B* **2024**, *853*, 138682. https://doi.org/10.1016/j.physletb.2024.138682.
10. Neves, J.C.S. Constraining the tidal charge of brane black holes using their shadows. *Eur. Phys. J. C* **2020**, *80*, 717. https://doi.org/10.1140/epjc/s10052-020-8321-z.
11. Ohashi, A.; Sakagami, M.A. Massive quasi-normal mode. *Class. Quantum Grav.* **2004**, *21*, 3973–3984. https://doi.org/10.1088/0264-9381/21/16/010.
12. Konoplya, R.A.; Zhidenko, A. Quasinormal modes of massive fermions in Kerr spacetime: Long-lived modes and the fine structure. *Phys. Rev. D* **2018**, *97*, 084034. https://doi.org/10.1103/physrevd.97.084034.
13. Konoplya, R.A.; Zhidenko, A. Asymptotic tails of massive gravitons in light of pulsar timing array observations. *Phys. Lett. B* **2024**, *853*, 138685. https://doi.org/10.1016/j.physletb.2024.138685.
14. Lütfüoğlu, B.C. Long-lived quasinormal modes and gray-body factors of black holes and wormholes in dark matter inspired Weyl gravity. *Eur. Phys. J. C* **2025**, *85*, 486. https://doi.org/10.1140/epjc/s10052-025-14210-0.
15. Bolokhov, S.V. Late time decay of scalar and Dirac fields around an asymptotically de Sitter black hole in the Euler–Heisenberg electrodynamics. *Eur. Phys. J. C* **2024**, *84*, 634. https://doi.org/10.1140/epjc/s10052-024-12990-5.
16. Skvortsova, M. Long-lived quasinormal modes of regular and extreme black holes. *Europhys. Lett.* **2025**, *149*, 59001. https://doi.org/10.1209/0295-5075/adaee2.
17. Dubinsky, A. Wave and particle probes of a regular T-duality-inspired black hole with gravitational self-energy. *arXiv* **2026**, arXiv:2607.07955. http://arxiv.org/abs/2607.07955v1.
18. Lütfüoğlu, B.C. Long-lived quasinormal modes, shadows and particle motion in four-dimensional quasi-topological gravity. *Eur. Phys. J. C* **2026**, *86*, 515. https://doi.org/10.1140/epjc/s10052-026-15807-9.
19. Skvortsova, M. Massive scalar quasinormal modes of an asymptotically flat regular black hole supported by a phantom Dirac–Born–Infeld field. *Ann. Phys.* **2026**, *492*, 170587. https://doi.org/10.1016/j.aop.2026.170587.
20. Lütfüoğlu, B.C. Long-lived quasinormal modes in the Euler–Heisenberg electrodynamics. *Phys. Lett. B* **2025**, *871*, 140026. https://doi.org/10.1016/j.physletb.2025.140026.
21. Skvortsova, M. Long-Lived Quasinormal Frequencies for Regular Black Hole Supported by the Einasto Profile in the Presence of the Magnetic Field. *Fortschr. Phys.* **2026**, *74*, e70142. https://doi.org/10.1002/prop.70142.
22. Bohra, S.S.; Sarkar, S.; Sen, A.A. Gravitational atoms in the braneworld scenario. *Phys. Rev. D* **2024**, *109*, 104021. https://doi.org/10.1103/physrevd.109.104021.
23. Deruelle, N.; Ruffini, R. Quantum and classical relativistic energy states in stationary geometries. *Phys. Lett. B* **1974**, *52*, 437–441. https://doi.org/10.1016/0370-2693(74)90119-1.
24. Damour, T.; Deruelle, N.; Ruffini, R. On quantum resonances in stationary geometries. *Lett. Nuovo Cimento* **1976**, *15*, 257–262. https://doi.org/10.1007/bf02725534.
25. Detweiler, S. Klein-Gordon equation and rotating black holes. *Phys. Rev. D* **1980**, *22*, 2323–2326. https://doi.org/10.1103/physrevd.22.2323.
26. Grain, J.; Barrau, A. Quantum bound states around black holes. *Eur. Phys. J. C* **2008**, *53*, 641–648. https://doi.org/10.1140/epjc/s10052-007-0494-1.
27. Barranco, J.; Bernal, A.; Degollado, J.C.; et al. Schwarzschild black holes can wear scalar wigs. *Phys. Rev. Lett.* **2012**, *109*, 081102. https://doi.org/10.1103/physrevlett.109.081102.
28. Baumann, D.; Chia, H.S.; Stout, J.; et al. The spectra of gravitational atoms. *J. Cosmol. Astropart. Phys.* **2019**, *2019*, 006. https://doi.org/10.1088/1475-7516/2019/12/006.
29. Leaver, E.W. An analytic representation for the quasi-normal modes of Kerr black holes. *Proc. R. Soc. Lond. A. Math. Phys. Sci.* **1985**, *402*, 285–298. https://doi.org/10.1098/rspa.1985.0119.
30. Leaver, E.W. Quasinormal modes of Reissner-Nordström black holes. *Phys. Rev. D* **1990**, *41*, 2986–2997. https://doi.org/10.1103/physrevd.41.2986.
31. Furuhashi, H.; Nambu, Y. Instability of Massive Scalar Fields in Kerr-Newman Spacetime. *Prog. Theor. Phys.* **2004**, *112*, 983–995. https://doi.org/10.1143/ptp.112.983.
32. Sampaio, M.O.P.; Herdeiro, C.; Wang, M. Marginal scalar and Proca clouds around Reissner-Nordström black holes. *Phys. Rev. D* **2014**, *90*, 064004. https://doi.org/10.1103/physrevd.90.064004.
33. Hod, S. Quasi-bound state resonances of charged massive scalar fields in the near-extremal Reissner–Nordström black-hole spacetime. *Eur. Phys. J. C* **2017**, *77*, 351. https://doi.org/10.1140/epjc/s10052-017-4920-8.
34. Kanti, P.; Konoplya, R.A.; Zhidenko, A. Quasinormal modes of brane-localized standard model fields. II. Kerr black holes. *Phys. Rev. D* **2006**, *74*, 064008. https://doi.org/10.1103/physrevd.74.064008.
35. Konoplya, R.A.; Zhidenko, A. Instability of D-dimensional extremally charged Reissner-Nordstrom(-de Sitter) black holes: Extrapolation to arbitrary D. *Phys. Rev. D* **2014**, *89*, 024011. https://doi.org/10.1103/physrevd.89.024011.
36. Abdalla, E.; Cuadros-Melgar, B.; Pavan, A.B.; et al. Stability and thermodynamics of brane black holes. *Nucl. Phys. B* **2006**, *752*, 40–59. https://doi.org/10.1016/j.nuclphysb.2006.06.017.